12
Dispersive G′-band and Higher-Order Processes: the Double Resonance Process

All kinds of sp^2 carbon materials exhibit a strong Raman feature which appears in the frequency range 2500–2800 cm^{-1}, as shown in Figure 1.5. Together with the G-band (1585 cm^{-1}), this higher-frequency feature in the spectrum is also a Raman signature of sp^2 carbon materials, and is called the G′-band[1)] to emphasize that it is a Raman-allowed mode for graphitic sp^2 carbons. Interestingly, the G′-band is a second-order two-phonon process and, intriguingly, it exhibits a strong frequency dependence on the laser excitation energy. This *dispersive behavior* ($\omega_{G'} = \omega_{G'}(E_{laser})$) is unusual in Raman scattering, since Raman-active mode frequencies usually do not depend on laser excitation energy. Together with many other Raman peaks (e. g., features around 2450 and 3240 cm^{-1} in Figure 4.14), the G′-band in sp^2 carbons pertains to the class of higher-order Raman spectra, which include overtone and combination modes (see Section 4.3.2.7). The G′-band in particular is a second-order process related to a phonon near the *K* point in graphene, activated by a double resonance process, which is responsible for its dispersive nature and causes a strong dependence on any perturbation to the electronic and/or phonon structure of graphene. For this reason, the G′ feature provides a very sensitive probe for characterizing sp^2 nanocarbons. For example, the G′-band can be used for differentiating between single and double-layer graphene with Bernal interlayer stacking order, as discussed in Section 4.4.3 and for probing aspects of the electronic structures of SWNTs. The present chapter discusses the science behind these higher-order Raman scattering processes and how they can be used to characterize sp^2 nanocarbons in general. In particular, we review in this chapter a number of the characteristics and properties of the most intense second-order feature in the Raman spectrum for sp^2 carbons, namely, the G′-band. In Section 12.1 the general aspects of higher-order Raman processes are considered, while in Section 12.2 double resonance phenomena are reviewed for graphene and generalized to other spectral features in Section 12.3. Strictly speaking, we should call this effect the "multiple-resonance process", since more than two resonances may take place, as discussed

1) The G′-band is also called the 2D band in the graphene literature. Here we use the conventional G′-band notation for the following reasons: (1) The G′-band is not a defect-induced process while the D and D′-bands denote defect-induced Raman features (see Chapter 13). (2) 2D is conventionally used to denote two-dimensional systems, and is so used also in the sp^2 carbon literature.

Raman Spectroscopy in Graphene Related Systems. Ado Jorio, Riichiro Saito, Gene Dresselhaus, and Mildred S. Dresselhaus

ISBN: 978-3-527-40811-5

in Section 12.2.1. However, most of the experimental results can be explained with the double resonance and, since it is largely treated in the literature with this name, we keep it here. The double resonance process in carbon nanotubes is discussed in Section 12.4, while Section 12.5 provides a brief summary of Chapter 12.

12.1 General Aspects of Higher-Order Raman Processes

A two-phonon emission process is a second-order Raman process, described classically by considering anharmonic terms in the polarizability tensor (see Section 4.3.1):

$$\alpha = \alpha_0 + \alpha_1 \sin \omega_q t + \frac{\partial^2 \alpha}{\partial Q_1 \partial Q_2} Q_1 Q_2 \,, \tag{12.1}$$

where Q_1 and Q_2 are amplitudes for the two phonons. The last term in Eq. (12.1) gives a Raman shift of $\pm\omega_1 \pm \omega_2$ for the two phonons.

In quantum mechanics, the two-phonon process is described by using fourth-order perturbation theory and the scattering intensity can be calculated using Eqs. (5.22) and (5.23), which are reproduced here:

$$I(\omega, E_{\text{laser}}) \propto \sum_i \left| \sum_{m',m'',\omega_1,\omega_2} J_{m',m''}(\omega_1, \omega_2) \right|^2 \,, \tag{12.2}$$

where the summation is taken over two intermediate electronic states m and m' and the corresponding phonon frequencies ω_1 and ω_2, and also for the initial states j, after taking the square of the scattering amplitude, $J_{m,m'}$ that is given by:

$$\begin{aligned} &J_{m',m''}(\omega_1, \omega_2) \\ &= \frac{M^d(\boldsymbol{k}, i\,m'') M^{\text{ep}}(-\boldsymbol{q}, m''\,m') M^{\text{ep}}(\boldsymbol{q}, m'\,m) M^d(\boldsymbol{k}, m\,i)}{(E_{\text{laser}} - \Delta E_{mi} - i\gamma_r)(E_{\text{laser}} - \Delta E_{m'i} - \hbar\omega_1 - i\gamma_r)} \\ &\quad \times \frac{1}{(E_{\text{laser}} - \Delta E_{m''i} - \hbar\omega_1 - \hbar\omega_2 - i\gamma_r)} \,. \end{aligned} \tag{12.3}$$

Equation (12.3) differs slightly from Eq. (5.23), by the addition of the broadening factor γ_r,[2] which gives the width of the resonance window, that is, the energy uncertainty related to the lifetime of the excited state, and avoids having J going to infinity when the system is in resonance. Figure 12.1 shows a Feynman diagram for a two-phonon Stokes Raman process. Of course, like for first-order processes in general (see Section 5.3), different scattering orderings are possible for this two-phonon process and each distinct process should be considered separately, using similar Feynman diagrams when making a very accurate intensity analysis of

2) In principle, the three γ_r factors in Eq. (12.3) can be different. However, there is no experimental evidence presently available to provide separate values for each of these γ_r factors.

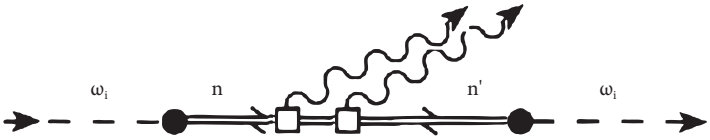

Figure 12.1 Feynman diagram for a two-phonon Stokes Raman process.

higher-order processes. In general, energy and momentum conservation for the incident (i) and scattered (s) electrons requires:

$$E_s = E_i \pm E_{q1} \pm E_{q2} \tag{12.4}$$

$$k_s = k_i \mp q_1 \mp q_2, \tag{12.5}$$

where $+$ $(-)$ in Eq. (12.4) and $-$ $(+)$ in Eq. (12.5) correspond to phonon absorption and emission with the wave vectors q_1 and q_2. By considering $k_s \approx k_i$ (see Section 4.3.2.6), momentum conservation requires $q_2 \approx -q_1$.

Any two-phonon scattering process involving the same Raman-active ($M^{\text{ep}} \neq 0$) phonon mode twice, and just obeying $q_2 = -q_1$ gives a Raman spectrum with a double frequency. Such a process can be observed for any solid. However, any $q \neq 0$ wave vector can be involved in two-phonon processes, and thus the corresponding Raman signal without any resonance effect is broad. Moreover, the anharmonic (or fourth-order) perturbation is relatively weak compared with the α_1 term in Eq. (12.1).[3] Interestingly, in sp^2 carbon materials the special electronic and phonon structures are such that resonance processes can take place for well-selected internal electron–phonon scattering processes. These resonance processes strongly enhance the second-order Raman spectra from specific phonons, through the so-called double resonance (DR) Raman process [159] described in Section 12.2. This then generates a unique Raman spectra for sp^2 carbon materials. There are two factors that govern the Raman intensity, thereby enhancing the probability of a scattering event for specific phonons:

1. The double resonance condition, which enhances J in Eq. (12.3) by minimizing two of the three factors in the denominator of Eq. (12.3) at the same time;
2. A strong electron–phonon matrix element, which enhances J by enhancing the numerator in Eq. (12.3).

The next sections discuss how these two factors occur in graphene (Section 12.2), and in carbon nanotubes (Section 12.4), focusing mostly on the G′-band, which is the most intense DR feature and is also one of the most dispersive features. Generalization of the DR process to many features in the Raman spectra of sp^2 nanocarbons is presented in Section 12.3.

3) This picture is different from higher-order Raman spectra for molecules, where the phonon amplitudes are large enough to enhance anharmonic effects and the electronic energy levels are discrete (and do not exhibit q-dependent effects).

12.2
The Double Resonance Process in Graphene

In this section the double resonance (DR) process introduced in Section 12.1 is reviewed for graphene, starting with a more detailed description of the double resonance process in Section 12.2.1. This is followed by a discussion of the dependence of this phenomenon on E_{laser} in Section 12.2.2 and on the number of layers of graphene in Section 12.2.3. Emphasis is also given in Section 12.2.4 to the use of the G′-band in characterizing graphene samples with regard to their stacking order along the c crystallographic axis.

12.2.1
The Double Resonance Process

When a photon with a given energy is incident on monolayer graphene, it will excite an electron from the valence band to the conduction band vertically in momentum space (gray arrow in Figure 12.2a). Since the graphene energy band does not have an energy gap, we always have an electron with wave vector k for any E_{laser} which satisfies $E_{\text{laser}} = E^{c}(k) - E^{v}(k)$. The photoexcited electron at k is then scattered by emitting a phonon with wave vector q to a state at $k - q$, as shown by the black arrow in Figure 12.2a. The phonon emission in Figure 12.2a corresponds to intervalley scattering in which the phonon q vector connects two energy bands at the K and K' points of the Brillouin zone. If there is a phonon in the vibrational structure of graphene with the wave vector q and phonon energy E_q so that this photon can connect the two conduction electronic states, this phonon scattering process will be resonant. A double resonance process (electron–photon and electron–phonon scattering, shown by the two solid dots in Figure 12.2a) will then take place.

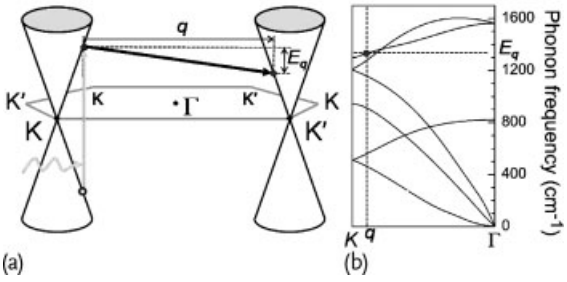

Figure 12.2 (a) This schematic diagram shows cones representing the electronic dispersion (energy vs. momentum) near the Fermi level at the K and K' points in the hexagonal Brillouin zone of graphene. The light-induced electron–hole formation and the one-electron–one-phonon scattering process taking place in the double resonance process are indicated by gray and black arrows, respectively. (b) The phonon dispersion in graphene is displayed [366], in which the phonon wave vector q measured from the Γ point and energy E_q are given by a dot.

Using a quantum mechanical description of this phenomenon, the two processes described above, and shown in Figure 12.2, give a large scattering amplitude J, since they minimize the first two terms in the denominator of Eq. (12.3). The full Raman process requires two phonons with wave vectors q and $-q$ for momentum conservation, and both the electron–hole creation by the incident photon and the subsequent electron–hole recombination by emitting scattered light are shown in Figure 12.3. In Figure 12.3, we show the corresponding intravalley two-phonon scattering processes in which the phonon q vector connects two conduction band states with the same K (or K') points. In graphene, both intravalley and intervalley (from/to K to/from K', see Figure 12.2) scattering processes can occur.

The processes shown in Figure 12.3a–c represent Stokes processes, where resonance with (a) the incident and (b) the scattered photons take place, in addition to the internal electron–phonon scattering process. While the electron–phonon resonant scattering shown in Figure 12.3b minimizes the second term in the denominator of Eq. (12.3), resonance with the incident/scattered photons minimizes the first/third term in the denominator of Eq. (12.3). Panels (d–f) of Figure 12.3 show the respective anti-Stokes processes. Note that, for the same laser excitation line, a different q vector will give rise to the double resonance process for Stokes and anti-Stokes processes ($q_S \neq q_{aS}$). A more detailed discussion can be found in [367].

The intervalley and intravalley double resonance two-phonon processes are, respectively, relevant near $2700\,\mathrm{cm}^{-1}$ (the G′-band), and near $3240\,\mathrm{cm}^{-1}$. The $3240\,\mathrm{cm}^{-1}$ peak arises from a second-order process for a $q \neq 0$ phonon near the maximum frequency in the phonon dispersion in Figure 12.2b near the Γ point,

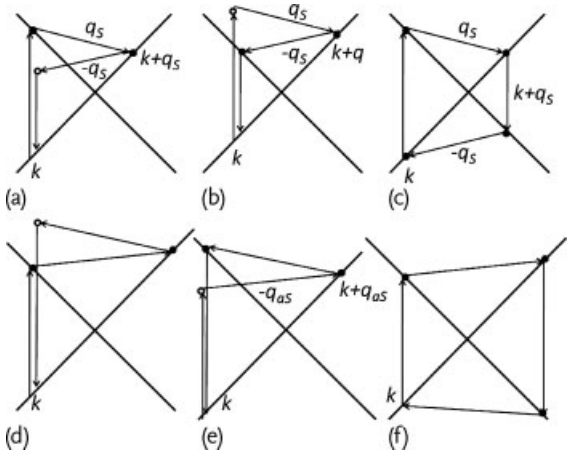

Figure 12.3 The full multiple resonance Raman process, with two electron–phonon scattering events, requiring both q and $-q$ phonons for momentum conservation, and the electron–hole recombination for scattered light emission. Double resonance with the incident light is shown in (a), while double resonance with the scattered light is shown in (b). Part (c) shows a fully resonant process, where the $-q$ scattering also takes place on the hole. Parts (a–c) are for Stokes (S) processes, while (d–f) show the corresponding anti-Stokes (AS) processes [160, 178, 367, 368].

for which the momentum transfer q is small in the intravalley process. The reason why the G′ feature is much more intense than the 3240 cm^{-1} feature has nothing to do with intravalley vs. intervalley scattering processes, but rather with the electron–phonon matrix elements, that are much stronger for phonons near the K point than for phonons near the Γ point.

Intriguing is the fact that the G′-band in mono-layer graphene is more intense than the first-order Raman-allowed G-band. Some argue that this is an indication that the dominating process is not the double-resonance but actually the fully-resonant scattering process shown in Figure 12.3c [369, 370]. However, this very strong G′-band intensity could also be related to different electron–phonon matrix elements for near K and near Γ point phonons. It is true that the fully resonant process in Figure 12.2c,f should, in principle, be much more probable than the others which exhibit a virtual (nonresonant) state. However, this is only valid if the electron and hole electronic dispersion relations are symmetric. Since the electron wave function overlap in graphene results in a different normalization for the valence and conduction bands, an electron–hole dispersion asymmetry is introduced, and for this reason the two processes could select DR phonons with somewhat different q vectors. This asymmetry is relatively small and is generally neglected in common descriptions of the electronic structure of graphene in terms of mirror band cones. More theoretical and experimental work is required to fully understand the differences in electron–phonon vs. hole-phonon scattering, including differences in the matrix elements that have not yet been addressed theoretically.

The slope of the energy dispersion $\partial E/\partial k$ is called the *group velocity*. When we consider only the direction of the group velocity for the initial k, there are two possibilities for scattered $k - q$ states as shown in Figure 12.4 where each of the intervalley (Figure 12.4a,c) and intravalley (Figure 12.4b,d) scattering processes correspond to backward (Figure 12.4a,b) and forward (Figure 12.4c,d) scattering. Here the backward (forward) scattering means that the direction of the group velocity

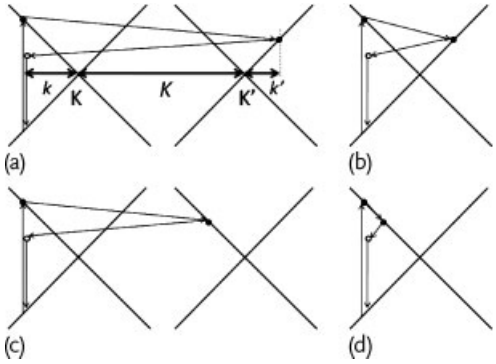

Figure 12.4 The double-resonance Stokes Raman processes for intervalley (a,c) and intravalley (b,d) scattering. Here (a,b) relates to the backward scattering process with $q_{DR} = k + k'$ and (c,d) relates to the forward scattering process with $q_{DR} = k - k'$, with k and k' measured from the K point. K is the distance between the K and K' points, k (k') is the distance of the resonant states from K (K'), as defined in (a) [160, 178, 367, 368].

does (does not) change after scattering. The corresponding q vectors for intervalley scattering are given by:

$$q = K + q_{\mathrm{DR}} = K + k + k' \approx K + 2k \quad \text{(backward scattering)} \tag{12.6}$$

$$q = K + q_{\mathrm{DR}} = K + k - k' \approx K \quad \text{(forward scattering)}\,, \tag{12.7}$$

where K is the distance between K and K', and k (k') here is measured from the K (K') point, which means q_{DR} is the phonon wave vector distance from the K (K') point. In the case of intravalley scattering, we just put $K = 0$ in Eq. (12.6) and (12.7). Since the phonon energy is usually small compared to the excited energy levels, $k \approx k'$, these two double resonance conditions approach $q_{\mathrm{DR}} = 2k$ and $q_{\mathrm{DR}} = 0$ (commonly used in the literature [158–160]). As already stated, the $q_{\mathrm{DR}} \approx 2k$ wave vector gives rise to the G′-band, while the $q_{\mathrm{DR}} \approx 0$ wave vector gives rise to a DR feature from the iTO phonon very close to the K point, consistent with the Raman peak observed around 2450 cm^{-1} in Figure 4.14 (see peak assignment summary in Chapter 14). However, there are some controversies about the origin of this 2450 cm^{-1} feature (denoted by G*), since ω_{G^*} is also consistent with the frequency of another combination mode, which is further discussed in Section 12.3. The $q_{\mathrm{DR}} \approx 0$ processes are expected to be less intense than the $q_{\mathrm{DR}} \approx 2k$ because the destructive interference condition is exactly satisfied for $q_{\mathrm{DR}} = 0$ [371]. However, the asymmetric (density of states-like) lineshape of the 2450 cm^{-1} feature in Figure 4.14 seems to be representative of the density of $\boldsymbol{q}$ vectors fulfilling the double resonance process, discussed in the next paragraph.

While all the important double resonance conditions have already been introduced, the picture discussed up to now is not the full story because graphene is a two-dimensional material. For a given laser energy, not only is the electron–hole excitation process shown in Figure 12.2 resonant, but any similar process within a circle in these cones defined by E_{laser} (see Figure 12.5) is also resonant. Furthermore, the mechanism of double resonance (DR) is actually satisfied by any phonon whose wave vector connects two points on two circles around K and K', as shown in Figure 12.5 [367]. (Here we neglect the trigonal warping effect of the constant energy surface of graphene near $K(K')$ for simplicity.) A phonon with wave vector q connects two points along the circles with radii k and k' around the K and K' points, respectively, where the difference between k and k' (for $k \neq k'$) comes from the energy loss from the electron to the phonon.[4] By translating the vector q to the Γ point, and considering all possible initial and final states around the K and K' points, the doughnut-like figure shown in Figure 12.5 is generated. Therefore, there is a large set of q vectors fulfilling the double resonance condition. However, there is also a high density of phonon wave vectors $\boldsymbol{q}$ satisfying the DR mechanism for which the end of the wave vectors measured from the Γ point are on the inner and outer circles of the "doughnut" in Figure 12.5. Therefore, the radii of the inner and outer circles around K'' (see Figure 12.5) are, respectively, $k - k'$ and $k + k'$.

4) Here q is the real phonon wave vector, measured from the Γ point, while in defining q_{DR}, k and k' are measured from K.

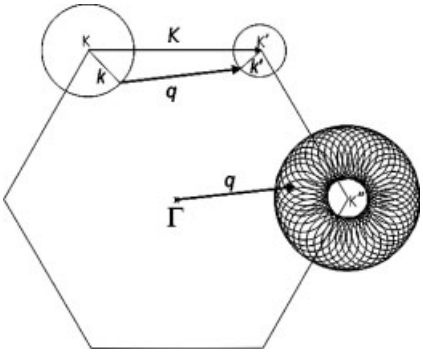

Figure 12.5 One of the possible double resonance (DR) Stokes Raman processes involving the emission of a phonon with wave vector $-\boldsymbol{q}$. The set of all phonon wave vectors $\boldsymbol{q}$ which are related to transitions from points on the two circles around K and K' gives rise to the collection of small circles around the K'' point obeying the vector sum rule $\boldsymbol{q} = \boldsymbol{K} - \boldsymbol{k} + \boldsymbol{k}'$ (here we neglect the trigonal warping effect). Note that this collection of circles is confined to a region between the two circles with radii $q_{\mathrm{DR}} = k + k' \approx 2k$ and $q_{\mathrm{DR}} = k - k' \approx 0$. The differences between the radii of the circles around K and K' and thus the radius of the inner circle around K'' are actually small in magnitude and are here artificially enlarged for clarity in presenting the concepts of the double resonance process [367].

Exactly as given by the 1D model (Eqs. (12.6) and (12.7)) these are the phonons associated with the singularities in the density of $\boldsymbol{q}$ vectors that fulfill the double resonance requirements, and they are expected to make a significant contribution to the second-order Raman scattering process. However, for a full description and lineshape analysis, considering the 2D model generates an asymmetric density of states that is consistent with the asymmetric lineshape that is observed for the 2450 cm^{-1} feature in Figure 4.14.

12.2.2
The Dependence of the $\omega_{G'}$ Frequency on the Excitation Laser Energy

As described in Section 12.2.1, when a photon with a given energy (E_{laser}) is incident on graphene, it will excite an electron from the valence to the conduction band. This electron can be resonantly scattered by a phonon with the correct wave vector q and phonon energy E_q to satisfy the double resonance conditions. Figure 12.6 shows that, if E_{laser} is changed, the correct wave vector q and phonon energy E_q that will fulfill the double resonance conditions will also change. This effect gives rise to the dispersive nature of the G′-band, which comes from an *intervalley* double resonance (DR) Raman process involving an electron with wave vector k in the vicinity of the K point and two iTO phonons with wave vectors $q_{\mathrm{DR}} \approx 2k$, where both k and q_{DR} are measured from the K point (see Section 12.2.1).

Figure 12.7a shows the Raman spectra in the region of both the G* (∼2450 cm^{-1}) and G′ (∼ 2700 cm^{-1}) bands for different laser excitation energies. Also the G*-band can be either explained by the $q \approx 0$ DR relation, or by the $q \approx 2k$ rela-

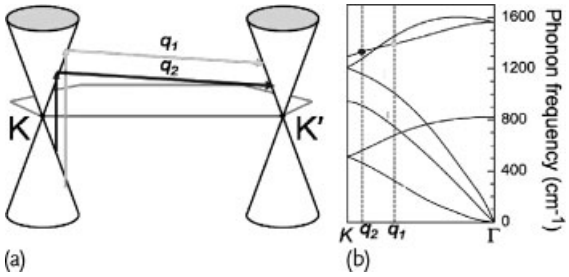

Figure 12.6 (a) The schematic diagram shows the light-induced electron–hole formation and one electron-one phonon scattering event taking place in the double resonance process with two different excitation laser energies (associated with phonon wave vectors q_1 and q_2, respectively), which are indicated by the gray and black arrows. (b) The phonon dispersion in graphene is shown where the phonon wave vector q that fulfills the double resonance requirements for each E_{laser} is also indicated in terms of the wave vectors q_1 and q_2.

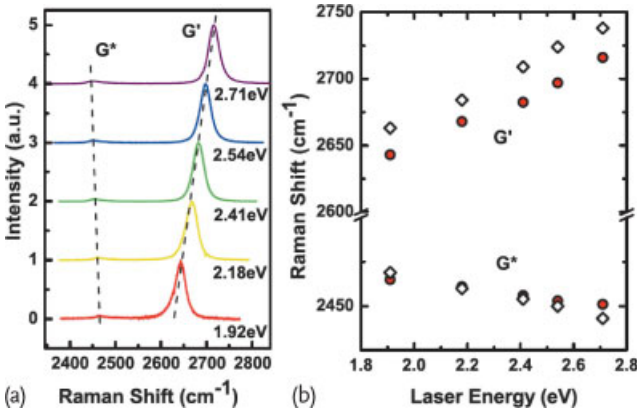

Figure 12.7 (a) Raman spectra of the G′ and the G*-bands of monolayer graphene for 1.92, 2.18, 2.41, 2.54 and 2.71 eV laser excitation energy. (b) Dependence of $\omega_{G'}$ and ω_{G^*} on E_{laser}. The red circles correspond to the graphene data and the lozenges correspond to data for turbostratic graphite. From [372].

tion applied to an *intervalley* process, but involving one iTO phonon and one LA phonon [371, 382]. Figure 12.7b shows the G′ and G* frequencies $\omega_{G'}$ and ω_{G^*} as a function of E_{laser} for graphene and turbostratic graphite (for which the stacking between graphene layers is random). The G′-band exhibits a highly dispersive behavior with $(\partial\omega_{G'}/\partial E_{\text{laser}}) \simeq 88\,\text{cm}^{-1}/\text{eV}$ for monolayer graphene, $95\,\text{cm}^{-1}/\text{eV}$ for turbostratic graphite [372], and $106\,\text{cm}^{-1}/\text{eV}$ for carbon nanotubes (see Section 12.4 and [173]). The G*-band exhibits a much less pronounced dispersion, with $(\partial\omega_{G^*}/\partial E_{\text{laser}}) \simeq -10$ to $-20\,\text{cm}^{-1}/\text{eV}$ and of opposite sign for both monolayer and turbostratic graphite [371, 372], and null for carbon nanotubes [373]. The G* feature is further discussed in Section 12.3.

To analyze the experimental data from Figure 12.7b, one has to consider the electron and phonon dispersion of a graphene monolayer, discussed in Chapters 2

and 3. Near the K point, the electron and phonon dispersions can be approximated by the linear relations $E(k) = \hbar v_F k$ and $E(q_{DR}) = \hbar v_{ph} q_{DR}$, respectively, where $v_F = \partial E(k)/\partial k$ and $v_{ph} = \partial E(q)/\partial q$ are the electron and phonon velocities near the K point, respectively (usually v_F is called the Fermi velocity, $v_F \sim 10^6$ m/s). The k (q_{DR}) is the electron (phonon) wave vector measured with respect to the K point, so that the general and approximated conditions for the double resonance Raman are given by:

$$\begin{aligned} E_{laser} &= 2v_F k \\ E_{ph} &= v_{ph} q_{DR} \\ q_{DR} &= k \pm k' \,, \end{aligned} \tag{12.8}$$

where E_{laser} and E_{ph} are, respectively, the laser and phonon energies, and k' is the scattered electron wave vector near the K' point in the graphene Brillouin zone. It is important to remember that we are dealing here with combination modes, so that the observed E_{ph} has to reflect this combination. For example, for the G′-band, the observed G′-band energy is given by $E_{G'} = 2E_{ph}$, where E_{ph} is the energy for the iTO phonon mode at q_{DR}.[5] Making another commonly used approximation in Eqs. (12.8), that is, $q_{DR} = k + k' \approx 2k$, then $E_{G'}$ can be written as:

$$E_{G'} = 2\frac{v_{ph}}{v_F} E_{laser} \,. \tag{12.9}$$

A drawback to the use of the DR Raman features to define the electron and phonon dispersion relations is that the measured values depend on both v_{ph} and v_F, and one has to be known to obtain the other. Adding to this problem, the physics of the phonon dispersion for graphene near the K point is rather complex due to the Kohn anomaly, which was discussed for the G-band ($q \to 0$) in Section 8.2, and the Kohn anomaly also occurs for phonons at $q \to K$. The high frequency of the iTO phonon when combined with the Kohn anomaly near the K point are together responsible for the strong dispersive behavior observed for $\omega_{G'}$. The exact values for v_{ph} and v_F are still under debate since they depend on the complex physics of many-body effects [86, 355, 366].

12.2.3
The Dependence of the G′-band on the Number of Graphene Layers

Because of the dispersive behavior of the G′-band, it can be used to characterize graphene layers in terms of their dispersive behavior and to distinguish between different types of graphene in terms of the number of layers and the stacking of these layers (see Figure 12.8). To explain this behavior, we first turn to the electronic properties of bilayer graphene with AB Bernal layer stacking (as also occurs in graphite), since this bilayer graphene structure is probed by resonance Raman

5) It is only when crystalline disorder is present that the first-order $q \neq 0$ phonons can be observed, as discussed in Chapter 13.

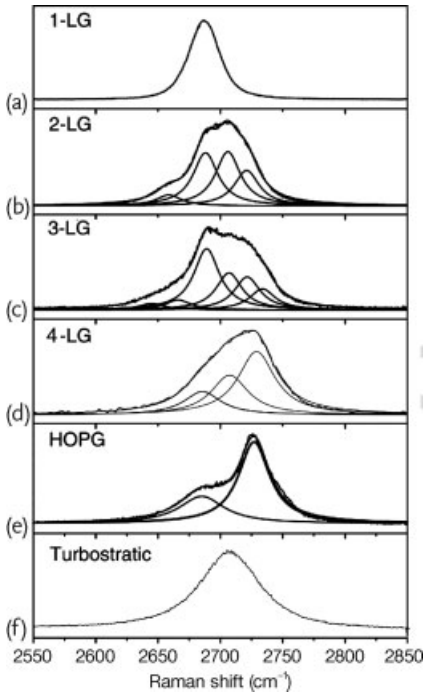

Figure 12.8 The G′ Raman band measured with $E_{\text{laser}} = 2.41\,\text{eV}$ for (a) 1-LG, (b) 2-LG, (c) 3-LG, (d) 4-LG, (e) HOPG and (f) turbostratic graphite. The splitting of the G′ Raman band opens up in going from mono- to three-layer graphene and then closes up in going from 4-LG to HOPG (see text) [84].

scattering. Since the electronic structure of graphene changes with layer stacking (see Section 2.2.4), such changes in layer stacking can be probed by the double resonance features, and most sensitively by the G′-band. Bilayer graphene has a richer G′-band spectrum (Figure 12.8b) than its monolayer counterpart (Figure 12.8a), because of its special electronic structure, consisting of two conduction bands and two valence bands (see Figure 12.9). From the double resonance (DR) Raman process in bilayer graphene with AB stacking, it is possible to distinguish four Lorentzians in the experimental Raman spectra for each laser line [86, 374]. The DR Raman model can then be used to relate the electronic and phonon dispersion of bilayer graphene with the experimental dependence of $\omega_{\text{G}'}$ on E_{laser} [192].

Figure 12.9a shows the dispersion of each one of the four peaks that comprise the G′-band as a function of E_{laser} for bilayer graphene, as shown in Figure 12.9b–e. Each one of the DR Raman processes obeying the selection rules (see Chapter 6) gives rise to one of the G′ peaks and is labeled as P_{ij} $(i, j = 1, 2)$ in Figure 12.9 [192], which connects two energy band E_i and E_j. Since the iTO phonon along the KM direction increases its frequency with increasing wave vector q, the highest frequency of the G′ peak for a given E_{laser} energy is associated with the P_{11} process, which also has the largest wave vector (q_{11}). The smallest wave vector q_{22}

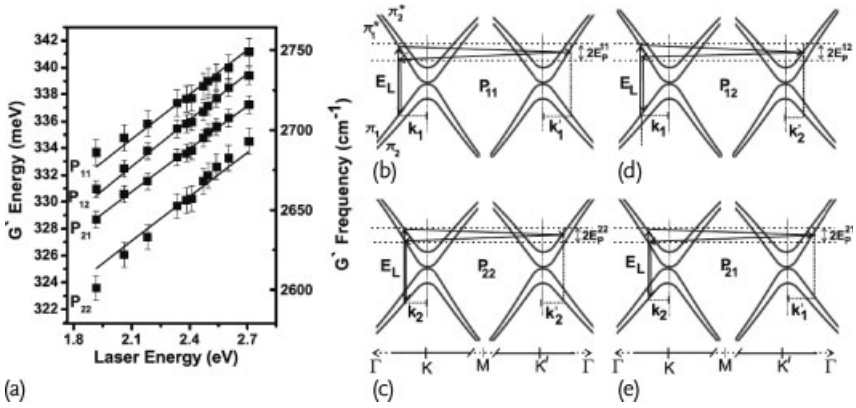

Figure 12.9 (a) Plot of the frequency of four peaks arising from the four G′-band peaks vs. E_{laser} observed in bilayer graphene. These four peaks arise from the four process shown in (b–e) to comprise the G′-band of bilayer graphene plotted in (a) as a function of laser energy [192].

is associated with the process P_{22}, which gives rise to the lowest frequency peak of the G′-band. The two intermediate frequency peaks of the G′-band are associated with processes P_{12} and P_{21} [192]. Increasing the number of layers increases the number of possible G′-band scattering processes. Trilayer graphene already has 15 possibilities [98, 217], but the frequency spacing between these peaks is not large enough to allow identification of each scattering event (Figure 12.8c). The situation gets even more complex for N-layer graphene ($N > 3$), though the G′-band spectra at a typical E_{laser} such as 2.41 eV starts to get simpler in appearance (Figure 12.8d for 4-LG), converging to a two-peak structure in highly oriented pyrolytic graphite (HOPG, $N \to \infty$, Figure 12.8e). The two-peak structure of the G′-band in HOPG (Figure 12.8e) is the result of a convolution of an infinite number of allowed DR processes in what turns out to be a three-dimensional electron and phonon dispersion. A geometrical approach for the understanding of the evolution of the G′-band in the Raman spectrum from monolayer graphene to bulk graphite (HOPG) has been discussed in [375].

12.2.4
Characterization of the Graphene Stacking Order by the G′ Spectra

A long time before graphene had been isolated, Raman spectroscopy had been used to quantify the structural ordering along the c axis in graphite, since the G′-band is very sensitive to the stacking order [155–157]. Nemanich and Solin were the first to show the change from one peak to two peaks in the profile of the G′-band in the Raman spectra obtained from polycrystalline graphite and crystalline graphite, respectively [150, 151]. Lespade *et al.* [155, 156] performed a Raman spectroscopy study on carbon materials heat treated at different temperatures T_{htt} and observed that, by increasing T_{htt}, the G′-band changes from a one peak to a two peak feature (see Figure 12.8e,f). They associated this evolution with the degree of

graphitization of the samples and suggested that the origin of the two-peak structure of the G′-band in crystalline graphite was related to the stacking order occurring along the *c* axis. Recently, the evolution of the G′-band from a single to a few graphene layers [86, 197, 374], and its complete evolution from the 2D to 3D aspect (from one to two peaks) has been quantitatively systematized (see previous section and [376]). Furthermore, Barros *et al.* have used the G′-band to identify three G′-band peaks due to the coexistence of 2D and 3D graphite phases in pitch-based graphitic foams [82].

Finally, it is important to mention that in CVD-grown graphene the stacking of the layers is often not AB Bernal stacking, and this lowering in symmetry results in a broadened single G′ peak for sample regions containing monolayer or bilayer graphene [71, 377, 378]. Thus the use of G′-band Raman spectroscopy to assign the number of layers needs to be viewed with caution since the G′-band lineshape is also strongly related to the stacking order of these layers.

12.3 Generalizing the Double Resonance Process to Other Raman Modes

The sp^2 carbons exhibit several combination modes and overtones, as shown in Figure 12.10 for graphite whiskers [379]. Basically all the branches in the phonon dispersion can be observed in such Raman features which obey the double resonance condition [160]. Many of the peaks observed in the spectra of Figure 12.10 below 1650 cm^{-1} are actually one-phonon bands activated by defects, as discussed in Chapter 13. Above 1650 cm^{-1} the observed Raman features are all multiple-order combination modes and overtones, some of which are also activated by defects.

As shown in Figure 12.10, the double resonance peaks change frequency with changing E_{laser}, and they can be fitted onto the phonon dispersion diagram shown in Figure 12.11 using DR theory (Section 12.2.2). The data points displayed in Figure 12.11 all stand for the $q_{DR} \approx 2k$ DR backward resonance condition, the ones near Γ and K coming from intravalley and intervalley scattering processes, respectively. Actually, in the Raman spectra there are no characteristic features distinguishing peaks associated with the intravalley from the intervalley scattering processes, or even from the $q_{DR} \approx 2k$ or $q_{DR} \approx 0$ resonance conditions. All we have in hand is the E_{laser} dependence of each peak that has to fulfill one of the DR processes and to fit the predicted phonon dispersion relations. For example, the data points near-K, assigned as the iTO+LA combination mode (TO + LA in Figure 12.11) could alternatively be assigned to a $q_{DR} \approx 0$ process, since this combination mode is very weakly (or non) dispersive [373]. Supporting this assignment is the asymmetric DR phonon-density of states-like shape observed for this peak, and against this identification is the destructive interference working towards DR Raman processes at exactly $q = K$ [129]. The debate about the iTO + LA combination mode assignment near the K point remains for future clarification. Near Γ the dispersive behavior is clear and the assignment is unquestionable [380].

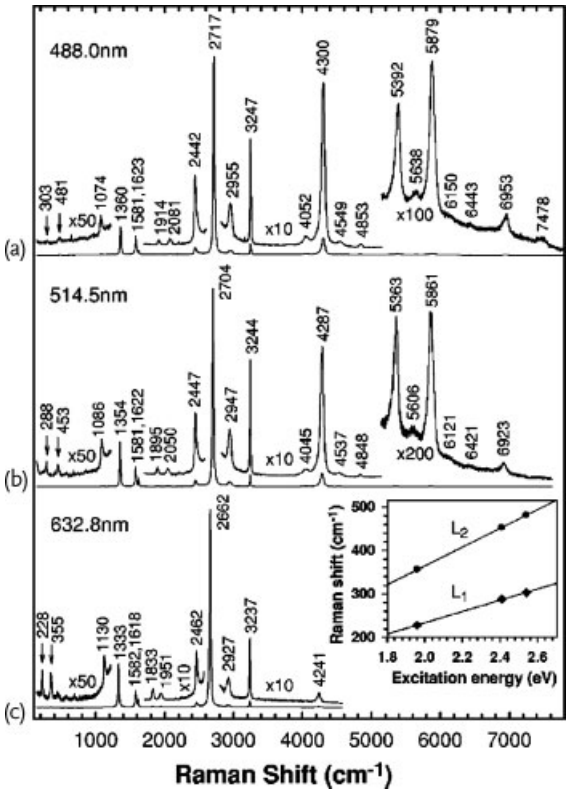

Figure 12.10 (a–c) Raman spectra of graphite whiskers obtained at three different laser wavelengths (excitation energies) [379]. Note that some phonon frequencies vary with E_{laser} and some do not. Above 1650 cm^{-1} the observed Raman features are all multiple-order combination modes and overtones, though some of the peaks observed below 1650 cm^{-1} are actually one-phonon bands activated by defects, as discussed in Chapter 13. The inset to (c) shows details of the peaks labeled by L_1 and L_2. The L_1 and L_2 peaks, which are dispersive, are explained theoretically by defect activation of double resonance one-phonon processes (see Chapter 13) involving the acoustic iTA and LA branches, respectively [160].

12.4
The Double Resonance Process in Carbon Nanotubes

For one isolated SWNT, the signal is limited to a fixed optical transition E_{ii} by the van Hove singularities, and we can say that the "dispersive" behavior will be "quantized". The effect of multiple bands of resonances can be seen in SWNT bundles where the vertical stripes in Figure 12.12a indicate resonance windows for a given resonance band. The modes appearing in Figure 12.12b for the spectral region between 400–1200 cm^{-1} are called intermediate frequency modes (IFMs), since their frequencies lie between the common RBM and G modes. The IFM features are attributed to combination modes (oTO $\pm$ LA [381, 382]), but it is not yet clear whether

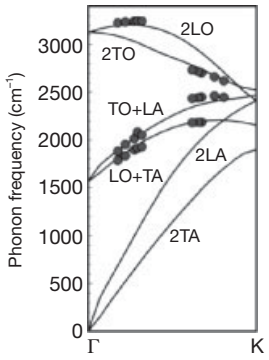

Figure 12.11 Two-phonon dispersion of graphite based on second-order double resonance peaks in the Raman spectra (circles). Solid lines are dispersion curves from *ab initio* calculations considering combination modes and overtones with totally symmetric irreducible representations. Adapted from [371].

these modes are Raman-active or induced by disorder (see Chapter 13). Theory relates their observation to quantum confinement along the tube length [383], and some supporting experimental evidence has been found for such an effect [384]. The IFM picture is not yet fully understood, but it represents a generalization of the double resonance effect. It is interesting to comment here that the DR theory for the dispersive features was actually developed for a one phonon inelastic scatter-

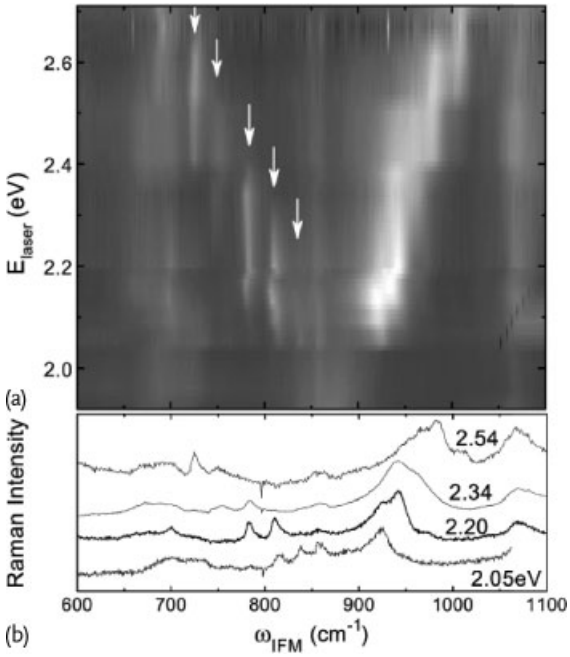

Figure 12.12 (a) Two-dimensional plot of the E_{laser} dependence for the Raman spectra of SWNT bundles in the intermediate frequency mode (IFM) range. The light areas indicate high Raman scattering intensity. Arrows point to five well-defined ω_{IFM} features. (b) Raman spectra in the IFM range taken with $E_{laser} = 2.05$, 2.20, 2.34, and 2.54 eV [381].

ing event plus one elastic scattering event activated by defects, such as the D-band, and this process is discussed in Chapter 13.

Like for the other sp^2 carbons, the G′ Raman feature in the carbon nanotube spectra provides unique information about the electronic structure of both semiconducting and metallic SWNTs. In analogy to graphene, SWNTs show dispersive behavior, although some unique characteristics are observed due to the one-dimensional structure of SWNTs. In Section 12.4.1 we show the G′ behavior in SWNT bundles, where most of the (n, m)-dependent uniqueness is averaged out, but there remains a close relation between SWNTs and graphene and some anomalous results can still be observed experimentally. In Section 12.4.2 we discuss the G′-band in isolated tubes, where anomalous effects related to their 1D structure are discussed. Regarding the analogy with multilayer graphene, carbon nanotubes have double-wall nanotubes (DWNTs), three-wall, MWNTs, etc. However, the literature on DWNTs is advancing rapidly and the complexity and richness associated with the differing properties of DWNTs having semiconducting vs. metallic outer and inner tubes make a detailed discussion of this large topic [289, 385, 386] outside the scope of this book. Many layers MWNTs exhibit large diameter nanotubes, thus approaching graphite [387].

12.4.1 The G′-band in SWNTs Bundles

SWNTs bundles exhibit behaviors not found at the individual tube level. Of particular interest is the novel dispersion of the G′-band observed in SWNT bundles. The inset to Figure 12.13a shows the dispersion of the $\omega_{G'}$ frequency in SWNT bundles. Fitting the observed linear dispersion with E_{laser} for SWNTs [173] gives:

$$\omega_{G'} = 2040 - 106\,E_{laser}\ . \tag{12.10}$$

However, different from graphene and graphite, the G′-band dispersion in SWNTs exhibits a superimposed oscillatory behavior as a function of E_{laser}, as shown in Figure 12.13a when the linear dispersion is subtracted from the data points. Such a behavior is not directly related to the uniqueness of the electronic structure, but rather is due to the $\omega_{G'}$ dependence on tube diameter.

The frequency of the measured G′-band feature depends on tube diameter because of a force constant softening, associated with the curvature of the nanotube wall that is dependent on d_t. Experiments on isolated tubes show the d_t dependence of $\omega_{G'}$ to be [389]

$$\omega_{G'} = \omega_{G'_0} - 35.4/d_t\ , \tag{12.11}$$

where $\omega_{G'_0}$ is the laser energy dependent value observed in graphene (the limit of an infinite diameter tube). This diameter dependence of $\omega_{G'}$ is responsible for the oscillatory behavior observed in Figure 12.13a. The vertical lines in Figure 12.13b denote the diameter range of the SWNT bundle used in the G′-band dispersion experiment. When moving along an arrow in Figure 12.13b by increasing the excitation laser energy, (for example, within the E_{22}^S sub-band by changing E_{laser}, above

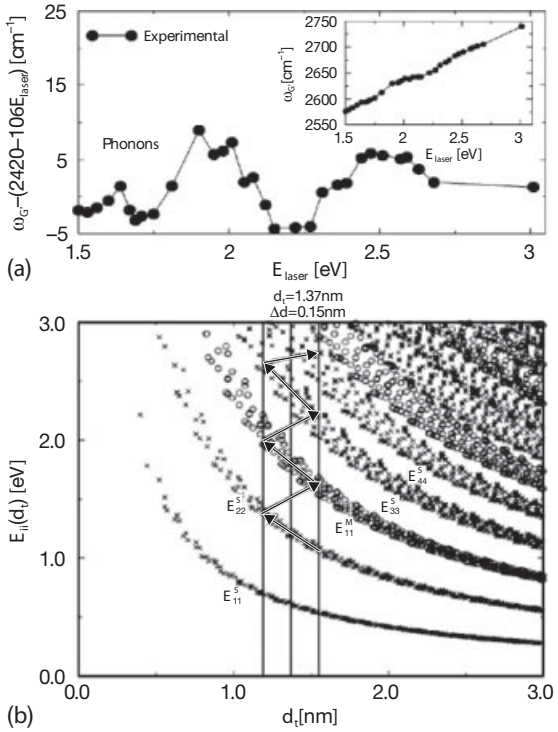

Figure 12.13 (a) Oscillatory dispersion G′-band data for $\omega_{G'}$ for a SWNT bundle sample taken from [173] after subtracting the linear dispersion $2420 + 106E_{laser}$ from the $\omega_{G'}$ vs. E_{laser} data shown in the inset. (b) Optical transition energies E_{ii} as a function of diameter for SWNTs (the Kataura plot). The vertical lines denote the diameter range 1.37+ or −0.15 nm of the SWNT bundle used in the G′-band dispersion experiment shown in (a) [388].

1 eV), different SWNTs with different diameters enter and leave resonance with a given E_{ii} optical transition. By increasing the laser energy, the diameter decreases, thus increasing the expected energy due to the double resonance process. When the resonance condition with E_{laser} jumps from, for example, E^S_{22} to E^M_{11} (around $E_{laser} = 1.5$ eV), the diameter jumps to higher values. This process modulates the $\omega_{G'}$ dispersion, as observed by the oscillatory behavior in $\omega_{G'}$ vs. E_{laser} seen in Figure 12.13a.

It is important to make clear that the "continuous" G′-band frequency dispersion observed in Figure 12.13 is a result observed in the bundles where different tubes enter and leave resonance, thus probing all the unfolded two-dimensional Brillouin zone. For one isolated SWNT, the signal is limited to a fixed optical transition E_{ii} by the van Hove singularities, and we can say that the "dispersive" behavior is quantized (see the results on the IFMs in Section 12.4, Figure 12.12). To fully appreciate the 1D-confinement effects on the G′ spectra, experiments on the isolated SWNT level have to be discussed, and this is the topic of Section 12.4.2.

12.4.2
The (*n*, *m*) Dependence of the G′-band

This section gives an appreciation of the effect of 1D confinement on the G′ feature in SWNTs. In the case of SWNTs, the resonance condition is restricted to $E_{\text{laser}} \approx E_{ii}$ (the transition energy between van Hove singular energies). This fact gives rise to a $\omega_{G'}$ dependence on the SWNT diameter (see Section 12.4.1) *and* chiral angle.

Figure 12.14 shows the cutting lines for two metallic SWNTs, one zigzag and one armchair, in the unfolded 2D Brillouin zone of graphene. The van Hove singularities occur where a cutting line is tangent to an equi-energy contour,[6] thus causing a chiral angle dependence on the excited states k_i, which are the states responsible for the dominant optical spectra observed for SWNTs, including the double resonance features. The presence of cutting lines in carbon nanotubes will, therefore, affect the dispersive Raman features [388] arising from the double resonance process [158–160]. The effects are general for many DR features (see Section 12.3), but we discuss here only the most intense double resonance Raman feature, the G′-band, since the G′-band dispersion is very large and, therefore, provides the most accurate experimental results for this effect.

The two-peak G′-band Raman features observed from semiconducting and metallic isolated nanotubes are shown in Figure 12.15a,b, respectively, where the (n, m) indices for these nanotubes are assigned as (15,7) and (27,3) [176]. The presence of two peaks in the G′-band Raman feature indicates the resonance with both the incident E_{laser} and scattered $E_{\text{laser}} - E_{G'}$ photons, respectively, with two different van Hove singularities (VHSs) for the same nanotube. E_{laser} and $E_{\text{laser}} - E_{G'}$ are defined in Figure 12.15a,b below the G′-band profiles, by the outer and inner equi-energy contours near the 2D Brillouin zone of the graphene layer. The wave vectors corresponding to the resonance VHSs are also shown. For the double resonance process in graphite, the momentum conservation for the electron–phonon interaction couples the electronic $\boldsymbol{k}$ and phonon $\boldsymbol{q}$ wave vectors by the relation $\boldsymbol{q} \approx -2\boldsymbol{k}$,[7] where both the electronic and phonon wave vectors are measured from

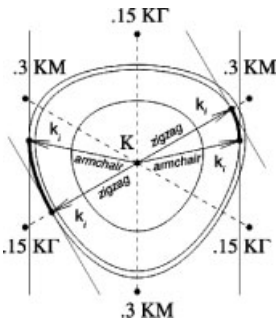

Figure 12.14 Cutting lines for two metallic SWNTs, one zigzag and one armchair, in the unfolded 2D Brillouin zone of graphene. The wave vectors k_i point with arrows to the locations where the van Hove singularities occur [390].

6) The equi-energies in Figure 12.14 have to include the trigonal warping effect to capture the full chirality dependence that is observed experimentally.
7) Equation (12.6) provides a consideration of the modulus only. The correct vectorial correlation between k and q would have a minus sign.

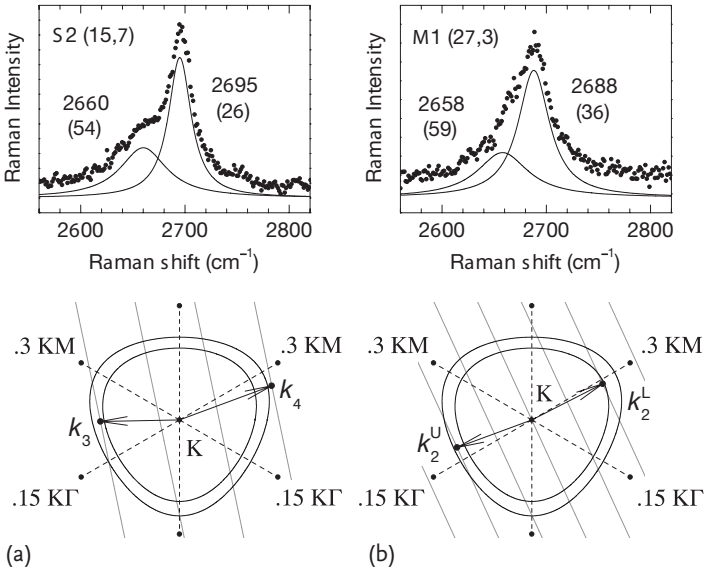

Figure 12.15 The G′-band Raman spectra for (a) a semiconducting (15,7) and (b) a metallic (27,3) SWNT, showing two-peak structures [390–392], respectively. The *vicinity* of the *K* point in the unfolded Brillouin zone is shown in the lower part of the figure, where the equi-energy contours for the incident $E_{\text{laser}} = 2.41\,\text{eV}$ and the scattered $E_{\text{laser}} - E_{G'} = 2.08\,\text{eV}$ photons, together with the cutting lines and wave vectors for the resonant van Hove singularities ($E_{33}^S = 2.19\,\text{eV}$, $E_{44}^S = 2.51\,\text{eV}$, $E_{22}^{M(L)} = 2.04\,\text{eV}$, $E_{22}^{M(U)} = 2.31\,\text{eV}$), are shown.

the nearest *K* point in the Brillouin zone [393]. For the double resonance process in carbon nanotubes, the introduction of cutting lines superimposed on the 2D Brillouin zone changes the equality relation $\boldsymbol{q} = -2\boldsymbol{k}$, which is slightly different in nanotubes relative to graphene or graphite because the allowed k vectors for carbon nanotubes are no longer continuous [390].

The two peaks in Figure 12.15a and b can be associated with the phonon modes of the wave vectors $\boldsymbol{q}_i = -2\boldsymbol{k}_i$, where $i = 3, 4, 2\text{L}, 2\text{U}$ for E_{33}^S, E_{44}^S, E_{22}^{ML}, and E_{22}^{MH}, respectively,[8] and the electronic wave vectors $\boldsymbol{k}_i$ are shown in the lower part of Figure 12.15. For the S-SWNT shown in Figure 12.15a, the resonant wave vectors $\boldsymbol{k}_3$ and $\boldsymbol{k}_4$ have different magnitudes, $k_4 - k_3 \simeq K_1/3$, resulting in twice the difference for the phonon wave vectors, $q_4 - q_3 \simeq 2K_1/3 = 4d_t/3$, so that the splitting of the G′-band Raman feature arises from the *phonon dispersion* $\omega_{\text{ph}}(q)$ around the *K* point. In contrast, for the metallic nanotube (M-SWNT) shown in Figure 12.15b, the resonant wave vectors $\boldsymbol{k}_2^{\text{L}}$ and $\boldsymbol{k}_2^{\text{H}}$ have roughly equal magnitudes and opposite directions away from the *K* point, so that the splitting of the G′-band Raman feature for metallic nanotubes arises from the *anisotropy* of the phonon dispersion $\omega_{\text{ph}}(q)$ around the *K* point [390], which we call the phonon trigonal warping effect. Overall,

8) The density of states of E_{22}^{M} for an M-SWNT splits into the two peaks (higher (H) and lower (L) energy peaks) except for armchair nanotubes, where a degeneracy in their frequency occurs.

the presence of two peaks in the double resonance Raman features of isolated carbon nanotubes is associated with quantum confinement effects expressed in terms of cutting lines. Correspondingly, the two-peak structure of the double resonance Raman features is not observed in 2D graphitic materials, such as in a monolayer graphene sheet. As stated above, the G′-band doublet structure observed in 3D graphitic materials is attributed to the interlayer coupling [157].

Finally, the G′-band is not the only feature to exhibit an (n, m) dependence for SWNTs. Actually, all the double resonance features may exhibit such a dependence. The stronger the dispersive behavior, the larger the (n, m) dependence. The smaller the tube diameter, the larger are the frequency shift effects. The (n, m) dependence of other combination modes, such as the iTO+LA combination mode near Γ, have been studied in detail (see [380]).

12.5 Summary

In this chapter we introduced the double resonance effect, important for explaining the observation of combination modes and overtones in sp^2 carbon materials. Many strong and weak Raman peaks can be assigned to two-phonon, second-order double resonance processes, while others are one-phonon disorder-activated processes, as discussed in Chapter 13. The peak frequencies usually exhibit small deviations depending on their sp^2 structure (single vs. multi-layer graphene, ribbons, tubes with different diameters and chiral angles, etc.), but in general the peak frequencies reflect the phonon dispersion relation of graphene subjected to the double resonance selection rules. This phonon dispersion effect allows us to probe the interior of the Brillouin zone with light scattering. Usually this is not possible using light because of the small momentum of photons as compared to the momentum range within the Brillouin zones of typical materials, so that neutron or electron scattering is generally applied to study such phenomena. The sensitivity to the detailed sp^2 structure makes these features, and especially the strong G′-band, a powerful tool for quantifying the number of graphene layers and the stacking order in graphite, and for studying various chirality-dependent effects in carbon nanotubes. The double resonance bands are strongly sensitive to changes in the electronic and vibrational structure in general, and serve as a sensitive probe for such effects.

Problems

[12-1] Polarization $\boldsymbol{P}$ is expressed by $\boldsymbol{P} = \alpha \boldsymbol{E}$, where is α is a polarization tensor, which is given by Eq. (12.1). When $\boldsymbol{E} = \boldsymbol{E}_0 \exp(i\omega t)$, $Q_i = Q_i^0 \exp(i\omega_i t)$, $(i = 1, 2)$, show that the last term of Eq. (12.1) gives the frequency terms of $\omega \pm \omega_1 \pm \omega_2$.

[12-2] In an optical process such as photoabsorption or phonon emission, the probability for the occurrence of an optical process is proportional to the square of the matrix elements of the electromagnetic perturbation in time-dependent perturbation theory. Explain how we get energy conservation and momentum conservation from perturbation theory. Especially show that these conservation rules are not always necessary because of the uncertainty principle, which becomes important for short times or short lengths.

[12-3] The $\pm$ symbols in Eq. (12.4) correspond to phonon absorption and emission with the wave vectors q_1 and q_2, respectively. Then explain, in the corresponding momentum conservation rule of Eq. (12.5), why we should not use $\pm$ but rather use $\mp$ by illustrating the scattering process in the two-dimensional Brillouin zone.

[12-4] Using Eqs. (12.2) and (12.3), analyze how the intensity of a second-order Raman process involving two phonons with q and $-q$ wave vectors changes when one, two or three denominators are minimized (select a constant value for γ_r and draw the resonance window). Make a comparative analysis of the intensities for the six processes depicted in Figure 12.3.

[12-5] Discuss how the triple-resonance process in Figure 12.3c,f depends on the symmetry between the valence and conduction band. For this discussion, show how the total intensity would change when the slopes for the electron and hole dispersions are different. Analyze the results as a function of γ_r and the phonon linewidth Γ_q.

[12-6] Since the electronic dispersion in graphene near the K point is characterized by a Fermi velocity of $v_F = 1 \times 10^6$ m/s and the G′-band dispersion is given by $(\partial\omega_{G'}/\partial E_{laser}) \simeq 88\,\mathrm{cm}^{-1}/\mathrm{eV}$, find the phonon dispersion for the iTO phonon branch in graphene. Compare the result you find with the result obtained by the force constant model described in Section 3.1.3. You will see why the addition of electron–phonon coupling, not accounted for in the force constant model, is very important for describing the phonon dispersion near the K point and, consequently, for explaining the dispersive behavior of the G′-band.

[12-7] Explain qualitatively how to obtain the circles around the K and K' points in Figure 12.5 by using the electron and phonon energy dispersion. Estimate the diameters of these circles for $E_{laser} = 2.41$ eV, and a phonon frequency of $1350\,\mathrm{cm}^{-1}$ and compare these lengths with the ΓK distance.

[12-8] Plot the phonon density of states as a function of energy for possible DR q vectors, as shown in Figure 12.5, by assuming that all circles are regular (not deformed) circles. Here assume that the phonon dispersion is proportional to the distance of q from the K point in the two-dimensional Brillouin zone.

[12-9] Considering the electron and phonon dispersions near the K point, calculate the difference in frequency between the Stokes and anti-Stokes process-

es for the G′-band (intervalley process), equivalent to the Stokes and anti-Stokes processes depicted in Figure 12.3a,d for the intravalley scattering process.

[12-10] Considering the double resonance condition $q \approx 0$, do you expect a dispersive (E_{laser}-dependent) behavior? Explain why.

[12-11] Draw a picture similar to Figure 12.5, but considering the trigonal warping effect. What differences do we expect to find in the double resonance features when the trigonal warping effect is included?

[12-12] Derive Eq. (12.9).

[12-13] Consider: (a) the average G′ dispersion ($\partial\omega_{G'}/\partial E_{\text{laser}}$) $= 106\,\text{cm}^{-1}/\text{eV}$; (b) the G′ diameter dependence given by Eq. (12.11); (c) the Kataura plot. Describe quantitatively the oscillatory behavior expected for the G′-band in SWNT bundles, considering a diameter distribution $1.2 \leq d_t \leq 1.6\,\text{nm}$ for the above three cases. For which diameter distribution would the oscillatory behavior become an averaged linear dispersion? Analyze your result as a function of the G′-band Raman peak width for one given SWNT.

[12-14] Explain how the inclusion of trigonal warping in the phonon dispersion relation would generate a chiral angle (θ) dependence for the G′-band of a hypothetical SWNT with the same d_t and as θ is changed from 0 to 30°.

[12-15] There is a mirror symmetry for n layer graphene (n is an odd number) in which a mirror is parallel to the graphene layer. The π energy band and phonon modes are either symmetric (S) or anti-symmetric (AS) with regard to the mirror operation. Discuss the selection rules for optical transitions and for the electron–phonon interaction for four possible combinations of S and AS energy bands. How about the case when n is an even number?

[12-16] When you look at Figure 12.3a,b, it is easy to see that the incident and scattered double resonance processes in graphene occur with the same $(q, -q)$ wave vector pair. Explain why two peaks are observed in the G′-band of SWNTs when both the incident and scattered light are in resonance with two different optical transition energies.

[12-17] Explain why there is no possibility of a second-order Raman process with the combination modes of two phonons, one causing an intravalley and one causing an intervalley scattering event.

[12-18] Explain that the density of states (DOS) of E_{ii}^{M} is split into two peaks from the two cutting lines near the K point except for armchair nanotubes. Please specify the cutting line in the two-dimensional Brillouin zone which corresponds to the DOS peak at the higher energy for each i of E_{ii}^{M}.